Comparison of simulated platform dynamics in steady/dynamic winds and irregular waves for OC4 semi-submersible 5MW wind-turbine against DeepCwind model-test results

H.C. Kim[*] and M.H. Kim

Civil Engineering, Texas A&M University, College Station, TX 77843, USA

Abstract. The global performance of the 5 MW OC4 semisubmersible floating wind turbine in random waves with or without steady/dynamic winds is numerically simulated by using the turbine-floater-mooring fully coupled dynamic analysis program FAST-CHARM3D in time domain. The numerical simulations are based on the complete second-order diffraction/radiation potential formulations along with nonlinear viscous-drag force estimations at the body's instantaneous position. The sensitivity of hull motions and mooring dynamics with varying wave-kinematics extrapolation methods above MWL(mean-water level) and column drag coefficients is investigated. The effects of steady and dynamic winds are also illustrated. When dynamic wind is added to the irregular waves, it additionally introduces low-frequency wind loading and aerodynamic damping. The numerically simulated results for the 5 MW OC4 semisubmersible floating wind turbine by FAST-CHARM3D are also extensively compared with the DeepCWind model-test results by Technip/NREL/UMaine. Those numerical-simulation results have good correlation with experimental results for all the cases considered.

Keywords: wind energy; FOWT (Floating Offshore Wind Turbine); OC4 semi-submersible; turbine-hull-mooring fully coupled dynamics; second-order wave diffraction QTF; FAST-CHARM3D; 5MW wind-turbine; viscous drag; wave-crest kinematics; Irregular waves; steady/dynamic wind

1. Introduction

To meet the increased demand of energy and reduce the CO_2 emission, ocean renewable energy sources need to be seriously considered in the future. Especially, offshore wind energy is appealing since it is economically competitive, technologically proven, infinitely renewable, and does not make any harmful waste or emission. Particularly, the wind quality in offshore region far from the coastal area becomes increasingly better and regulatory restriction is much less there. In this regard, several countries installed offshore floating wind turbines (Dominique *et al.* 2010) in relatively deeper water. Although they are considered to be more difficult to design than fixed offshore wind turbines, floating wind turbines have many advantages compared to onshore or bottom fixed offshore wind turbines. If the technology is completely developed, floating offshore wind turbines

---

∗Corresponding author, Ph.D. Student, E-mail: doriduul@tamu.edu
[a] Professor, E-mail: m-kim3@tamu.edu

are expected to be more popular to generate considerable amounts of clean renewable energy at competitive prices compared to other energy sources (Henderson *et al.* 2002, Henderson *et al.* 2004, Musial *et al.* 2004, Tong 1998, Wayman *et al.* 2006).

One of the challenging issues on the floating offshore wind turbine is the survivability in extreme sea conditions. From design/analysis aspect, the most difficult part is the coupled dynamics analysis among the mooring system, floating platform, and wind turbine. Therefore, for reliable design and technology development, it is necessary to develop the integrated tool to accurately analyze the fully coupled dynamics including control. Some efforts are in progress toward this direction for several selected types of floating offshore wind turbines. In this paper, the global performance analysis of the OC4 5-MW semi-submersible floating wind turbine (e.g., Robertson *et al.* 2012) is investigated by the fully coupled dynamic analysis tool CHARM3D-FAST, the combination of FAST (e.g., Jonkman 2004) developed by NREL and CHARM3D (e.g., Yang and Kim 2010, Kang and Kim 2012) developed by the second author's research group (e.g., Bae and Kim 2011, 2014).

For the OC4 semi-submersible case, Masciola *et al.* (2013) analyzed the system by including only linear wave force and using quasi-static or lumped-mass methods for mooring model. Also, Coulling *et al.* (2013a,b) performed the validation for the semi-submersible platform including second-order wave-diffraction forces based on Newman's approximation. However, the mooring model in the analysis was also quasi-static, so the true dynamic coupling between hull and mooring lines was missing in the study. Recently, Koo *et al.* (2014a) analyzed the OC4 semisubmersible wind turbine and compared their numerical predictions by their own code, MLTSIM-FAST, against DeepCWind model test results. Moreover, the second-order wave-diffraction effects were briefly introduced and discussed in their work (Koo *et al.* 2014b). A more detailed study with respect to the effects of the complete second-order diffraction/radiation solutions including comparisons against simplified methods was conducted by authors (Kim and Kim 2015). On the other hand, Zhao and Wan (2015) carried out motion simulations of the OC4 semi-submersible platform in waves by using their own CFD code, naoe-FOAM-SJTU. For the 3-column semisubmersible with similar hull shape called "Windfloat" (Dominique *et al.* 2010), the wind turbine is not mounted at the center but on one of the three columns with the other two columns water ballasted. The offshore system has successfully been installed and operated in full scale in Portugal.

In the present study, the fully coupled wind-turbine/hull/mooring dynamics numerical model developed for the OC4 semi-submersible system (Kim and Kim 2015) including viscous and complete second-order difference-frequency wave effects is further utilized to investigate sensitivity with empirical parameters and response characteristics for more diverse environmental conditions including steady and dynamic winds. All the simulation results were systematically compared against the corresponding experimental results, which shows reasonably good agreement among them. Additionally, the effects of the extrapolated wave crest kinematics above MWL and the role of steady/dynamic winds and viscous/aerodynamic damping on the 6DOF motions and mooring top tensions are discussed.

2. Numerical simulation in time domain

In order to solve a wind turbine on a single floating platform, FAST (e.g., Jonkman and Buhl Jr. 2004), developed by National Renewable Energy Laboratory (NREL), was modified and extended

so that it can calculate the full coupled dynamics among wind turbine, floating platform, and mooring lines. The coupled dynamic responses between the turbine and floater can be derived from the full-DOF matrix equation including floater 6-DOFs and wind-turbine multi-DOFs with proper platform-turbine coupling terms. The combined left-hand-side matrix with the given forcing functions in the right-hand side is solved at each time step. Assuming that every degree of freedom for a three-bladed turbine in FAST is turned on, the total DOFs, for example, can be expressed as 6 (for floater) +19 (for turbine)=25. The coupled terms between the floating platform and turbine in the coefficient matrix can be derived by accounting for every effect of generalized inertia and active forces from both bodies. The detailed theory and equations are given in Bae and Kim (2014)

Between the floater and mooring line dynamics, the necessary data exchange is also done at each time step for their dynamic coupling. The hydro-dynamic loadings and instantaneous tensions for mooring lines are obtained from CHARM3D (e.g., Kim *et al.* 2001, Tahar and Kim 2003, Yang and Kim 2010) along with viscous forces on Morison members and convolution-integral forces for floater. They are fed to FAST at each time step. The transferred external forces include first-order and second-order wave forces. Then FAST fills out the forcing function of the platform DOFs using those transferred forces, and solves displacements, velocities, and accelerations of all the degrees of freedom including elastic responses of towers and blades. The obtained platform displacement and velocity data are then fed into CHARM3D side to update the relevant external forces. The instantaneous velocites of the platform are used for the next-time-step convolution–integral term. The instantaneous positions of the platform's Morison members are used for viscous drag forces with instantaneous incident-wave kinematics. The transferred instantaneous positions of the mooring-connection points are used as an input for the next-time-step mooring dynamics and resulting tension. The basic concept of rotor-floater coupling is schematically shown in Fig. 1.

3. Second-order wave loads and convolution integral in time domain

In this section, the time-domain realization of the first- and second-order wave forces/moments in a random sea is explained. The first- and second-order hydrodynamic forces/moments on a floating body caused by stationary Gaussian random seas can be written as a two-term Volterra series in the time domain as follows

$$F^{(1)}(t) + F^{(2)}(t) = \int_{-\infty}^{\infty} h_1(\tau)\eta(t-\tau)d\tau + \int_{-\infty}^{\infty}\int_{-\infty}^{\infty} h_2(\tau_1,\tau_2)\eta(t-\tau_1)\eta(t-\tau_2)d\tau_1 d\tau_2 \qquad (1)$$
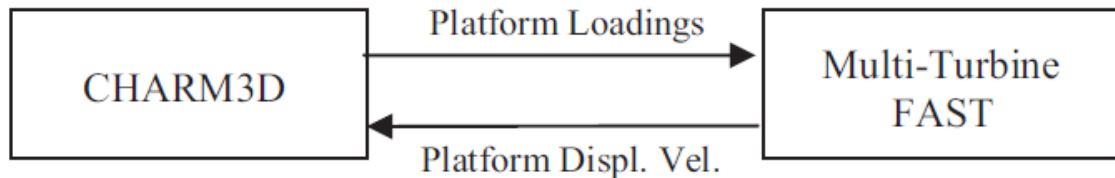

Fig. 1 Basic concept of FAST-CHARM3D coupling

Where $\eta(t)$ is the ambient wave free surface elevation at a reference position, $h_1(t)$ is the linear impulse response function, and $h_2(\tau_1, \tau_2)$ is the quadratic impulse response function. The above equation can also be expressed in the form of the summation of N frequency component waves as below

$$F_I^{(1)}(t) = Re\left[\sum_{j=1}^N A_j L(\omega_j) e^{i\omega t}\right] \tag{2}$$

$$F_I^{(2)}(t) = Re\left[\sum_{j=1}^N \sum_{k=1}^N A_j A_k^* D(\omega_j, -\omega_k) e^{i\omega^- t}\right] \tag{3}$$

Where $L(\omega_j)$ represents the linear force transfer function (LTF), *A* is complex wave amplitude, and $D(\omega_j, -\omega_k)$ is the difference-frequency quadratic transfer functions (QTF). The sum-frequency second-order forces/moments are not included in (3) since they play little role for the overall dynamics of semisubmersible platform.

The radiation-potential-induced force/moment in time domain can be expressed as follows

$$F_R(t) = -M^a(\infty)\ddot{\zeta}(t) - \int_{-\infty}^t R(t - \tau)\dot{\zeta}(\tau)d\tau \tag{4}$$

Where ζ is platform motion, upper dot is time derivative, $M^a(\infty)$ is the added mass of platform at infinite frequency, and $R(t)$ is retardation function (or time-memory function), which is related to the frequency-domain solutions of the radiation problem as follows

$$R(t) = \frac{2}{\pi} \int_0^\infty C(\omega) \cos(\omega t) d\omega \tag{5}$$

Where $C(\omega)$ is the radiation-wave-induced damping coefficient at frequency ω.

The total wave loads in time domain can then be written by summing all the force components as below.

$$F_{total}(t) = F_I(t) + F_R(t) \tag{6}$$

where the total wave exciting force $F_I(t) = F_I^{(1)}(t) + F_I^{(2)}(t)$.

4. DeepCwind semisubmersible wind-turbine model description

Table 1 and Fig. 2 show the floating platform properties and DeepCwind offshore wind-turbine geometry, respectively. The property in Table 1 is about only the floating platform, and the wind turbine part is not included. The wind turbine is based on NREL 5 MW baseline turbine (Jonkman *et al.* 2007), but it is modified for a 1/50th scale model test. (Coulling *et al.* 2013a).

5. Numerical modeling

The x-axis symmetry is used and the half of the wet hull is discretized by 3600 panels. Panels near the free surface are more finely modeled as shown in Fig. 3. The free-surface discretization is also needed in the complete second-order diffraction/radiation problem (Kim and Yue 1989, 1990) A total of 4888 panels are used for the free-surface discretization up to the truncated radius of 80m (Kim and Kim 2015). The convergence test with a finer mesh are carried out and it was checked that the added mass, radiation damping, and linear- and second-order wave forces were converged

satisfactorily for the present application. It was concluded in Kim and Kim (2015) that the best agreement against measurement was achieved when the complete second-order diffraction/radiation solutions were used. For the present application, only the second-order difference-frequency wave forces are relevant and thus the sum-frequency part is not considered. The potential-based hydrodynamic coefficients and excitations are first calculated by WAMIT in frequency domain, and they are subsequently used for time-domain simulations for FAST-CHARM3D. Also, the viscous force is added using drag-force formula for all the Morison members including the braces that connect columns to pontoons. Since the crossflow drag forces are proportional to relative velocities squared, they can contribute to both excitation and damping. The viscous drag forces on Morison members above MWL are also evaluated at each time step by using the instantaneous wave kinematics extrapolated from the values at MWL. In this study, both uniform and linear extrapolations are used for that purpose. Since the nonlinear viscous drag forces are evaluated at the instantaneous platform positions, they also contribute to nonlinear motion components with higher harmonics. As for the potential forces, the fluctuation of the free surface along the hull waterline is considered in the second-order diffraction/radiation formulations.
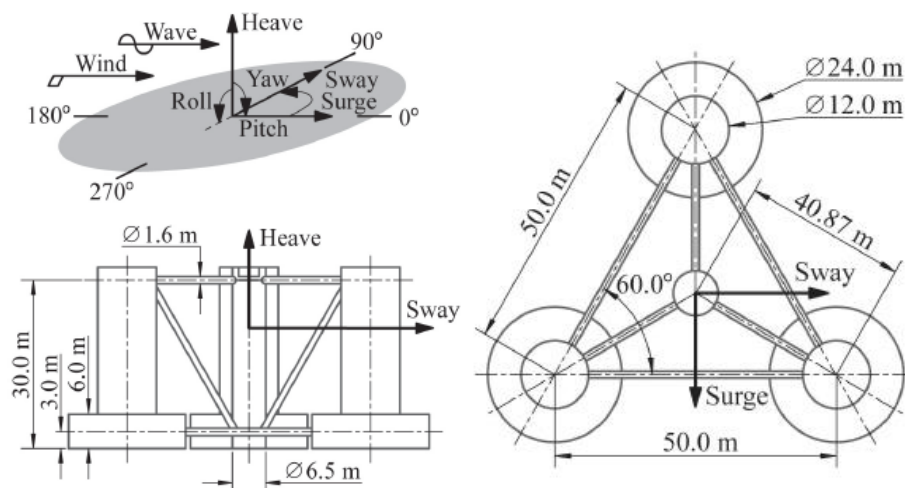

Fig. 2 DeepCwind Semisubmersible platform geometry front view (left) and Top view (right) (Coulling *et al.* 2013a)

Table 1 offshore floating platform property

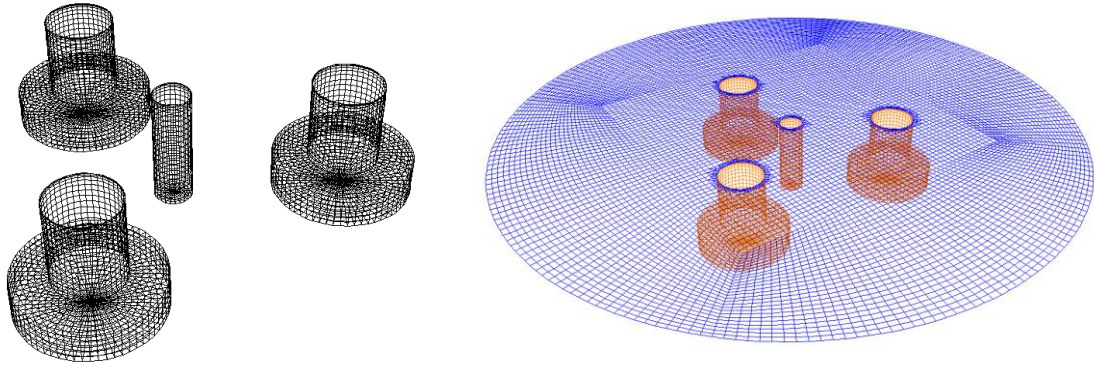| ITEM	Unit	Value
Platform Center of Mass	m	-14.4
Platform Mass	ton	1.3444E+04
Platform Inertia Ixx, Iyy	kg-m^2	8.0110E+09
Platform Inertia Izz	kg-m^2	1.3910E+10
Nacelle and blade Mass	ton	397.1
Tower Mass	ton	302.2

Fig. 3 Numerical model of OC4 platform (left) and free surface panels (right) for potential-flow calculation

6. Wind turbine modeling

The adopted model of 5 MW turbine is the 'National Renewable Energy Laboratory (NREL) offshore 5 MW baseline wind turbine'. In the model test, the wind blades were designed to be nearly rigid and thus the flexibility option of the blades was turned off in the simulation. The flexibility of the tower is included by using a linear modal representation as suggested in ARTP. Two fore-aft and two side-to-side mode shapes of tower are used for hull-turbine-mooring coupled dynamic analysis. The natural frequencies of the first tower fore-aft mode and first tower side-to-side mode are 2.20 and 2.39 rad/sec respectively (Coulling *et al*. 2013a). The natural frequencies of those elastic modes are much higher than the wave and floater-motion frequencies. The tower base is located at the 10m height from the MWL, so the flexibility of tower begins from that height. The details of the tower-blade-control models can be found in Bae and Kim (2014). It is well known that in the case of semisubmersible-type floater, the flexibility of tower plays less critical role in overall coupled dynamics compared to the TLP-type floater (Bae and Kim 2011).

7. Mooring modeling

The mooring system is composed of omni-spread three catenary lines. The mooring-line modeling was done by a pre-processor HARP of CHARM3D code. To satisfy the static equilibrium, the total buoyancy of the platform should be the same as the sum of the total structure weight and the vertical-component tension of the mooring system, as shown in Table 3. The high-order finite rod-element method is used for the mooring dynamics modeling, the details of which are given in Kim *et al*. (2001) and Tahar and Kim (2003). The drag coefficient used for the chain mooring is 2.4. The mooring line property is tabulated in Table 2, and the anchor points are tabulated in Table 4. By comparing physical/numerical static offset tests, it was confirmed that the mooring system was correctly modeled (see Fig. 6 of Kim and Kim 2015)

Table 2 Mooring properties

Mooring Type		Chain
Mooring Axial Stiffness	MN	753.6
Unstretched Mooring Line Length	m	835.5
Mooring Mass Density (Dry)	kg/m	113.35
Mooring Mass Density (Wet)	Kg/m	108.63
Seabed Friction Coefficient		1
Mooring Drag Coefficient		2.4
Mooring Added-Mass Coefficient		1

Table 3 vertical-plane static equilibrium

Platform + Tower Weight(N)	1.38703E+08
Buoyancy(N)	1.40589E+08
Total Vertical Tension(N)	1.88612e+06

Table 4 Anchor points

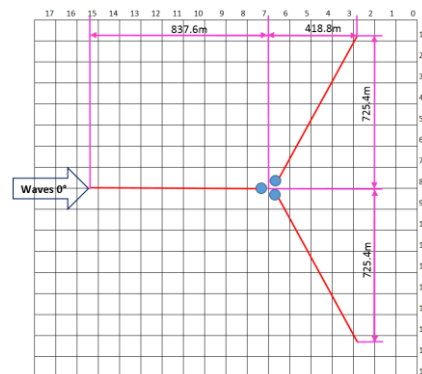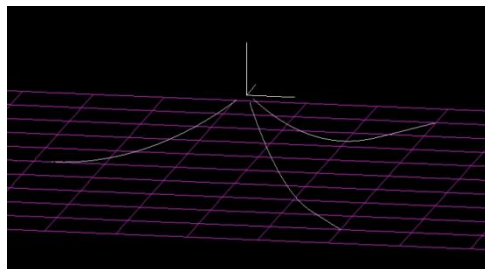| #1 Anchor Point	:	(418.8,	725.4,	-200)
#2 Anchor Point	:	(-837.6,	0,	-200)
#3 Anchor Point	:	(418.8,	-725.4,	-200)

Fig. 4 Mooring system modeling by HARP (left) and the mooring arrangement (right)

8. High white noise case (Hs=10.5m, T=6~25sec)

The same white-noise wave spectra with Hs = 10.5 m and T=6~25 sec as in the experiment, were inputted into FAST-CHARM3D time-domain simulation program. Then the corresponding irregular waves are generated through FAST-CHARM3D. 100 wave components were used with the random perturbation of component central frequencies to avoid signal repetition (Kim and Yue 1991). The comparisons between the regenerated wave spectrum from the simulated time series and the counter-part in measurement are shown in Fig. 5. The corresponding statistics are

tabulated in Table 5. The predicted and measured data generally agree well having similar trend except that the experimental incident waves have more nonlinear features (higher crest and shallower trough).

A sensitivity test with varying wave crest kinematics was also conducted as shown in Fig. 6. Uniform- and linear-extrapolation techniques, which are popular empirical wave kinematic models above MWL (Longridge *et al*. 1996), are selected to obtain more realistic representation of wave kinematics above MWL. In addition, no extrapolation case is also added to see the effect of the wave crest kinematics above MWL. The wave kinematics obtained from both techniques are applied to the Morison equation for the moving body, and the drag forces on Morison members were evaluated accordingly at the instantaneous body position and up to the instantaneous free-surface elevation at every internal time step. The velocities are squared in computing the drag force as Eq. (7), thus the different wave-kinematics-extrapolation techniques can make appreciable differences in the motion results, especially in slowly varying surge motions

$$F_d = \frac{1}{2} \rho\, C_d\, A\, (u - v)\, |u - v| \tag{7}$$

where *u* and *v* are wave velocity and body velocity respectively, *A* is projcted area, and C_d is drag coefficient.

For illustration, surge drag coefficient for the cylindrical columns 1.6 and heave drag coefficient for the column footing 3.2 were selected. Those drag coefficients were decided from the comparison between numerical and experimental free-decay tests, as shown in Kim and Kim (2015). Fig. 6 shows the mentioned two extrapolation methods. In the case of surge, the slowly varing motions are equally or more important than wave-frequency motions although there is no incident wave energy at that low frequency. The low-frequency motions are caused by nonlinear wave excitations including the diffrence-frequency second-order wave forces. The extrapolation of the wave kinematics has appreciable effect on the slowly varing surge motions. When the extrapolation above MWL is not applied, the resulting slowly varying surge response is under-estiamted compared to the experimental values. However, when the uniform or linear extrapolation is applied, the surge spectrum is much closer to the experimental surge spectrum. When the linear extrapolation is applied, the simulated surge spectrum (or surge standard deviation) best matches with the measured one. However, when surge mean offset is considered, the uniform extrapolation method gives better comparison against experimental value, as can be seen in Table 7. In this regard, from this point on, uniform extrapolation method is adopted.

In the case of pitch, the pitch spectrum in the simulation is slightly under-estimated compared to the measurement pitch data near the peak. It may be caused by higher crest and shallower trough of experimentally generated waves, as shown in Table 5. Nevertheless, the overall trend is very similar between the measurement and numerical prediction. The mean pitch is slightly overpredicted by the simulation. As a matter of fact, it is almost impossible to have an intially perfect vertical position of the model in the experiment due to complex cable arrangment. Also, under the ideal model set-up, the sway and roll are supposed to be zeros in head waves but they were not negligible in the model test, which may also contribute to the differences.

In the case of heave, unlike the surge case, the first-order wave-frequency motions are dominant over the second-order slowly-varying motions and there is generally good agreement between the simualtion and experiment including the peak magnitude. Heave natural frequency is located at 0.36rad/sec as shown in Table 6. The heave damping mostly comes from the column footing and it was modeled by a disk Morison member at its mid position. Its admping coefficient

Cd=3.2 was determined from heave free-decay test. A more sophisticated Morison member modeling of the footing by using upper and lower locations during the upward and downward heave motions was also tested and it led to almost the same results. The wave kinematics extrapolation methods little affect the heave motions because it mostly has an effect on the surge force near the free surface. The comparison of the taut-side mooring top tension between the simulation and measurement shows good agreement, which warrants the correctness of the numerical/physical modeling of mooring lines. Since the wave-frequency dynamics are dominant in mooring tension, a full dynamic approach has to be used instaed of a quasi-staic approach.

Table 5 Generated wave statistics

Wave(m)	White Noise			
	Max	Min	Mean	SD
Exp	12.814	-11.008	-0.034	2.853
Sim	10.03	-11.64	0	2.845

Table 6 Comparison of the surge, heave, and pitch natural frequencies between simulation and model test

DOF	Natural frequencies(rad/sec)	
	FAST-CHARM3D	Model Test
Surge	0.0556	0.0555
Heave	0.3605	0.3641
Pitch	0.2381	0.2277

Table 7 Surge, heave, and pitch motions and mooring top tension statistics

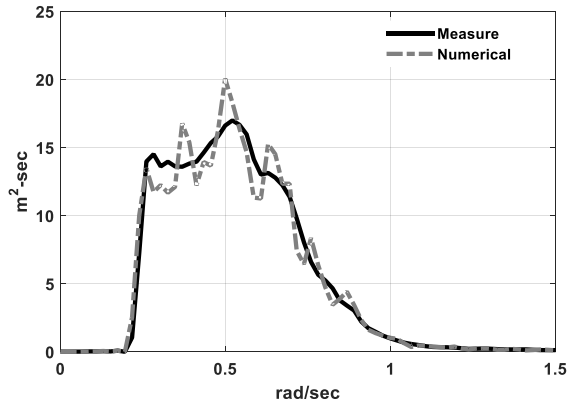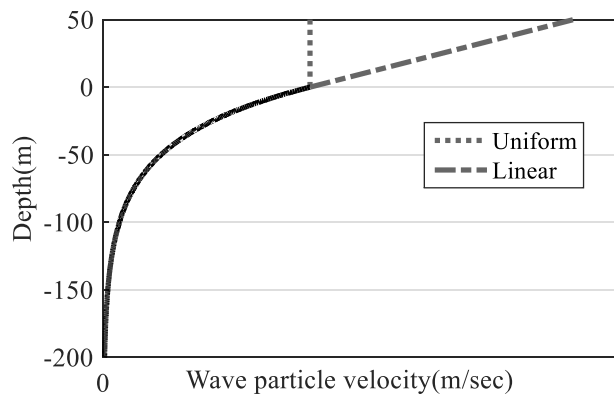| Title	Unit	Extrapolation	Max	Min	Mean	SD
Surge	m	Exp	17.878	-5.008	3.363	3.040
		Linear	15.725	-4.756	5.049	3.010
		Uniform	14.449	-4.711	4.495	2.731
		No Ext.	11.451	-4.674	2.833	2.172
Heave	m	Exp	5.993	-6.399	0.042	1.741
		Linear	5.904	-5.788	0.180	1.811
		Uniform	5.907	-5.789	0.181	1.812
		No Ext.	5.908	-5.776	0.182	1.813
Pitch	deg	Exp	6.465	-7.243	0.061	1.627
		Linear	5.632	-5.886	0.132	1.414
		Uniform	5.180	-6.018	0.120	1.422
		No Ext.	5.633	-6.366	0.097	1.471
Mooring Top Tension	kN	Exp	5867.0	38.7	1347.3	484.3
		Linear	4599.8	-145.0	1389.7	507.2
		Uniform	4330.0	-140.1	1348.5	472.0
		No Ext.	3653.3	-150.7	1241.0	394.0

Fig. 5 High white noise wave spectrum

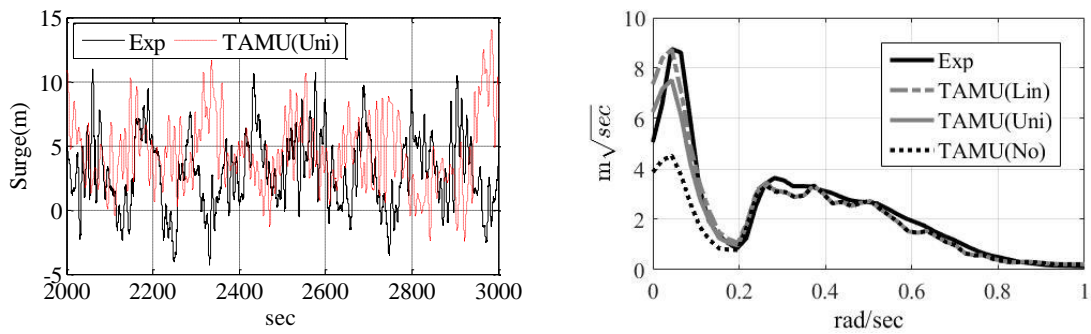Fig. 6 Uniform and linear wave crest kinematics

Fig. 7 Surge time series (left) and square root of spectra(SRS) (right) in the high white noise case in various wave kinematics
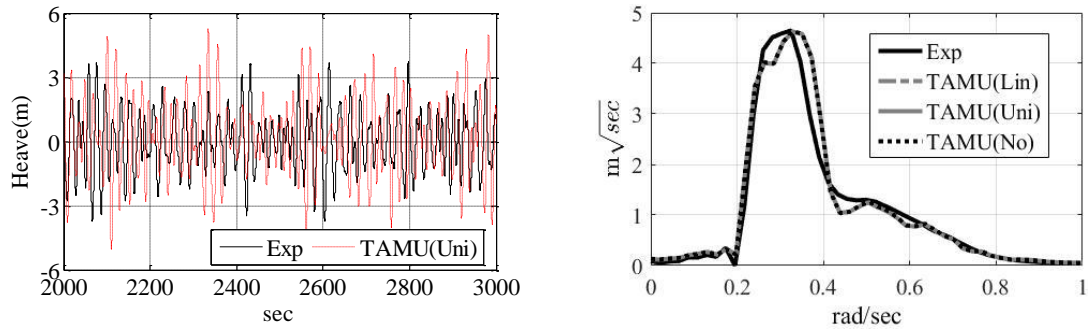
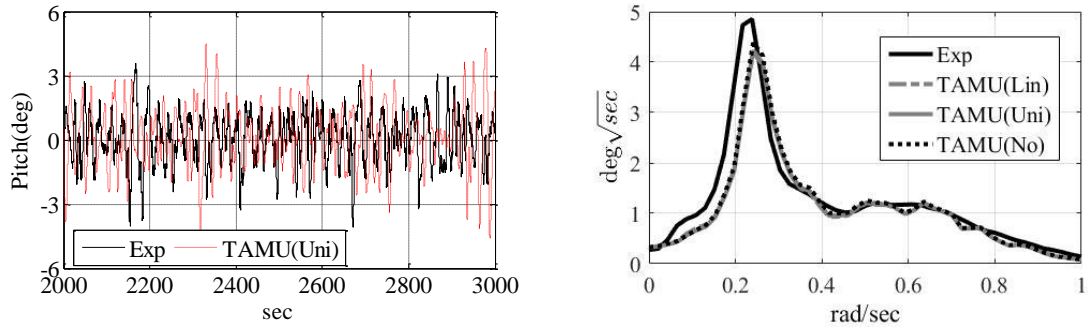Fig. 8 Heave time series (left) and SRS (right) in the high white noise case in various wave kinematics

Fig. 9 Pitch time series (left) and SRS (right) in the high white noise case in various wave kinematics
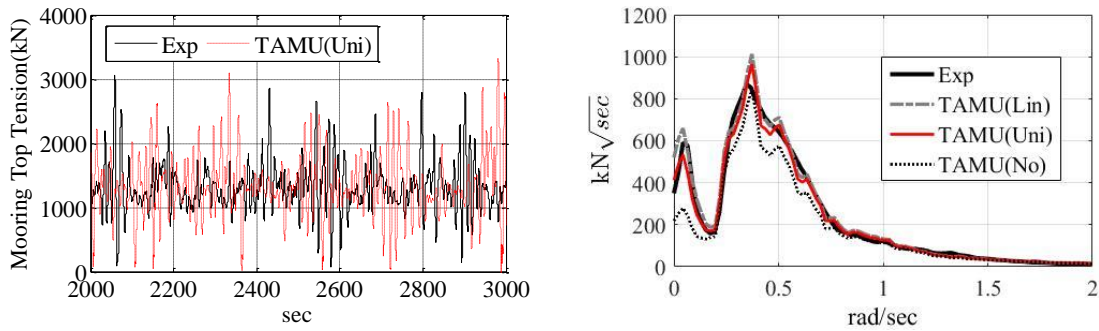

Fig. 10 Taut-side mooring top tension time series (left) and SRS (right) in the high white noise case in various wave kinematics

9. Only irregular wave condition (Hs=7.1m, Tp=12.1sec)

Next, the simulation/experiment with more realistic wave spectrum for only irregular wave condition is considered. The environmental condition is 7.1m siginificant wave height and 12.1 sec

peak period with enhancement parameter=2.2. From this case, the uniform extrapolation is used for the wave kinematics calculation above mean water level. Fig. 11 shows comparisons among the model-test wave spectrum, the regenerated wave spectrum in simulation, and the theoretical input JONSWAP spectrum. They agree very well as shown in the Fig. 11. The environmental conditions are tabulated in Table 8. The wave related statistics are tabulated in Table 9. We also see that the experimentally generated incident waves are more nonlinear than simulated ones characterized by higher crest and shallower trough.

Figs. 12-15 show the surge, heave, pitch, and mooring-tension spectra and time series, and the corresponding statistics are tabulated in Table 10. In this simulation, the sensitivity with varying column drag coefficients is tested. The previous column drag coefficient Cd=1.6 was obtained from the first two cycles of the surge free-decay test. If subsequent cycles with smaller amplitudes were used, its value would be decreased. In this regard, the results with Cd=0.8 are also presented.

Table 8 Environmental condition and drag coefficient in the irregular wave condition

Title	Unit	Value
Significant Height (Hs)	m	7.1
Peak period (Tp)	sec	12.1
Gamma (enhancement parameter)		2.2
Column Drag coef.		1.6
Footing Heave Drag coef.		3.2

Table 9 Wave amplitude statistics

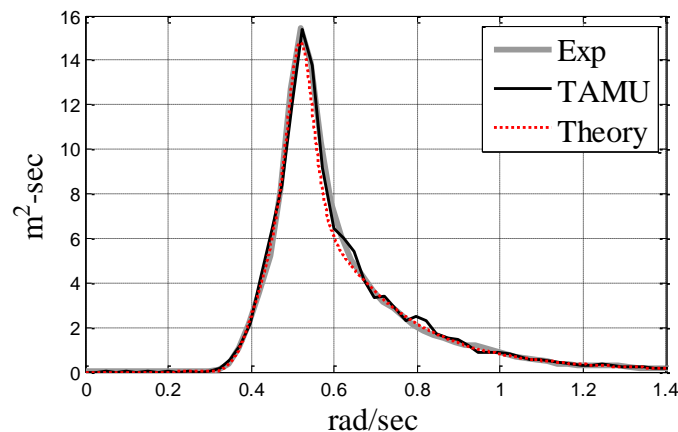| Title	Unit		Max	Min	Mean	SD
Wave Amplitude	m	Exp	7.741	-6.452	-0.008	1.784
		TAMU	7.133	-6.806	0.000	1.789

Fig. 11 Comparison of wave power spectrum among experiment, simulation, and theory

It turns out that there is little difference in motion and tension spectra between the two cases, which means that the corresponding sensitivity of floater motions and mooring tensions against the selected range of column drag coefficient is small. When mean surge is compared against measurement, Cd=0.8 is better. However, when surge standard deviation is concerned, Cd=1.6 is better (see Table 10). There is almost no change between the two cases for heave and pitch modes. From this point on, Cd=1.6 is used. The general trend of comparison between the numerical and experimental results is similar to that of the previous white-noise-spectrum case. In general, the numerical simulations successfully recover the general characteristics of motion and tension spectra with small differences in magnitudes. The causes of the small differences are analogous to those of the previous case. We can also see that there exists high correlation between the motion and mooring-tension results.

Table 10 Surge, heave, and pitch motions and mooring top tension statistics

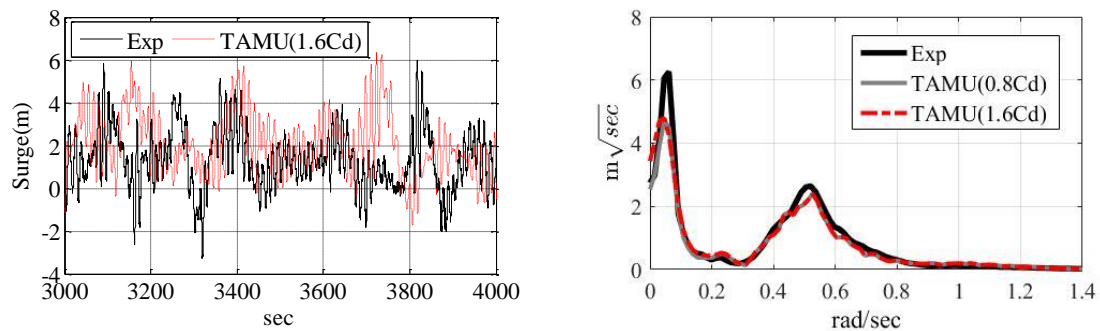| Title	Unit	Extrapolation	Max	Min	Mean	SD
		Exp	9.199	-3.923	1.352	1.730
Surge	m	Uniform(0.8Cd)	6.975	-3.335	1.607	1.455
		Uniform(1.6Cd)	8.022	-2.639	2.079	1.547
		Exp	2.450	-2.121	0.006	0.520
Heave	m	Uniform(0.8Cd)	2.583	-1.678	0.129	0.504
		Uniform(1.6Cd)	2.586	-1.674	0.129	0.503
		Exp	3.321	-3.948	0.032	0.863
Pitch	deg	Uniform(0.8Cd)	2.426	-2.711	0.024	0.685
		Uniform(1.6Cd)	2.428	-2.640	0.025	0.678
		Exp	2682.3	231.6	1221.5	168.7
Mooring Top Tension	kN	Uniform(0.8Cd)	2222.6	493.1	1182.9	133.3
		Uniform(1.6Cd)	2365.5	547.9	1208.8	144.8

Fig. 12 Surge time series (left) and SRS (right) in the irregular wave
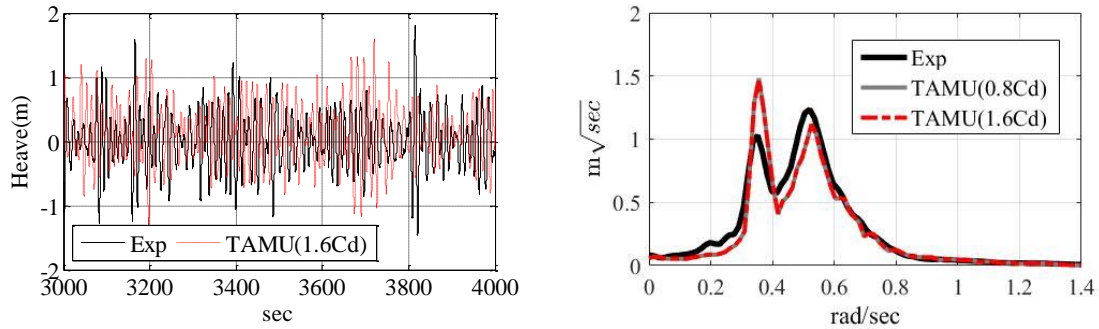
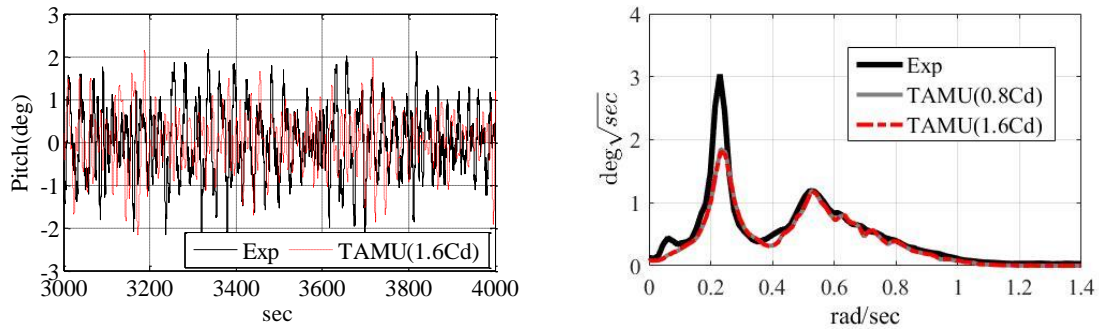Fig. 13 Heave time series (left) and SRS (right) in the irregular wave

Fig. 14 Pitch time series (left) and SRS (right) in the irregular wave
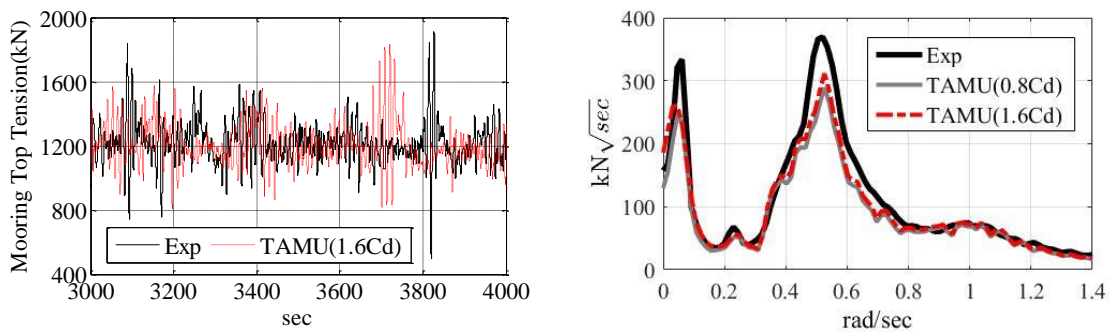

Fig. 15 Taut-side mooring top tension time series (left) and SRS (right) in the irregular wave

10. Irregular wave + Steady wind condition (Hs=7.1 m, Tp = 12.1 sec, Wind Speed at hub = 16.11 m/sec)

Next, 16.11 m/sec steady wind at hub height is added to the irregular wave condition of the previous section. In order for the same thrust to be given to the rotor as in the experiment, the blade pitch angle in the numerical simulation is fixed at 12.34 deg. When the 16.11m/set steady

speed is given, the calculated thrust is 382.0kN, which is almost the same as the measured thrust of 381.7kN converted to the full scale in the model test. When only the steady wind is given excluding the wave, the surge and pitch offsets, taut-side mooring top tension, and fore-aft tower base bending moment are slightly smaller than the measurement values. Their differences are small as shown in Table 11, which shows that the steady-wind effect is reasonably modeled in the simulation. Figs. 16 and 17 show the surge, heave, pitch, and taut–side top mooring tension amplitude spectra when the irregular wave and the steady wind coexist at the same time, and the corresponding statistics are tabulated in Table 12. The overall spectral trend is very similar to that of the previous section. When the steady wind is added, the biggest change occurs in mean surge offset (increased from 2.1 (or 1.4) m to 6.7(or 5.9) m in simulation(or in experiment)) and mean pitch inclination (increase from 0.03 to 1.9 degrees in both simulation and measurement). Due to the large increase in surge offset, along with the corresponding hardening property of the mooring line stiffness (see Fig. 9 of Kim and Kim 2015), the surge stiffness changes and it affects the reduction of the slowly-varying surge amplitudes, which can be observed both in simulation and measurement. The shift of mooring stiffness also influences the increase of wave-frequency dynamic mooring top tension, as observed both in simulation and measurement. Another factor that reduces surge and pitch slowly-varying motions at the corresponding resonance peaks after adding the steady wind is aerodynamic damping. Since aero dynamic force on blades is proportional to the relative velocity squared between the wind and platform, there exists aero damping even though wind velocity is constant. The addition of steady wind little influences the heave mode. Both simulated and measured results demonstrate such trends.

Table 11 Comparison of model test and simulation steady-state response for surge, pitch, taut side mooring top tension, and fore-aft bending moment under steady 16.11m/sec wind at hub height

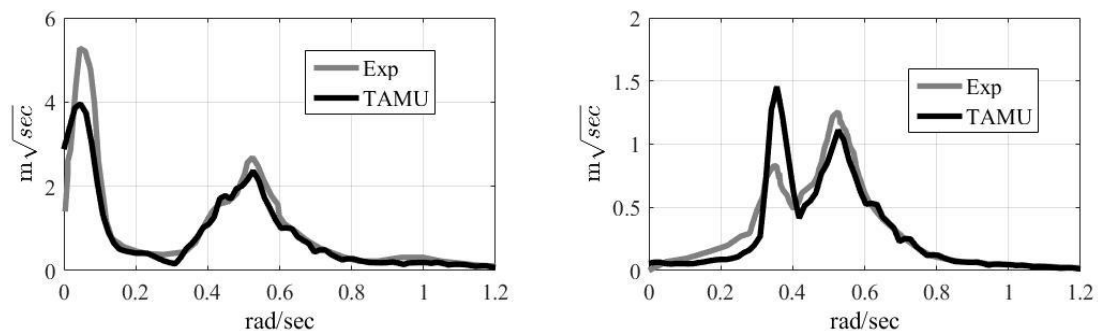| Title	Unit	model test	Simulation
Surge	m	5.260	5.025
Pitch	deg	1.967	1.849
Mooring Top tension	kN	1394.0	1371.4
Fore-aft bending moment	kN-m	47030	46070

Fig. 16 Surge SRS (left) and Heave SRS (right) in the irregular wave and steady wind condition
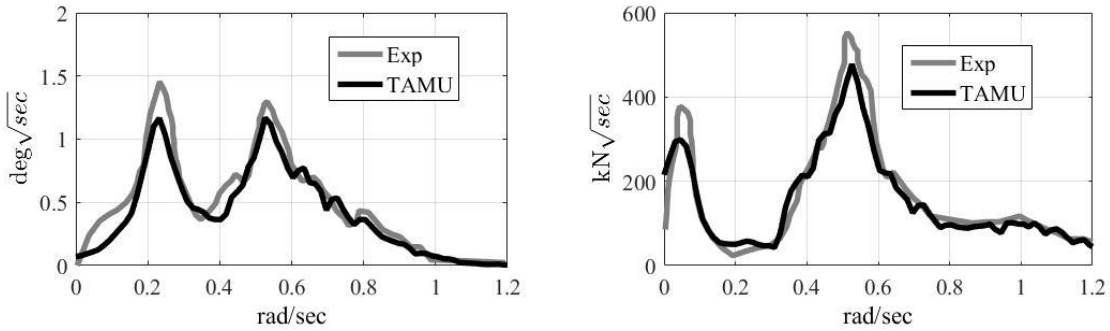
Fig. 17 Pitch SRS (left) and Taut-side mooring top tension SRS (right) in the irregular wave and steady wind

Table 12 Surge, heave, and pitch motions and mooring top tension statistics

Title	Unit	Extrapolation	Max	Min	Mean	SD
Surge	m	Exp	14.100	1.530	5.900	1.590
		Uniform(1.6Cd)	12.413	2.386	6.724	1.408
Heave	m	Exp	2.170	-2.160	N/A	0.482
		Uniform(1.6Cd)	2.536	-1.720	0.071	0.501
Pitch	deg	Exp	4.900	-1.170	1.870	0.686
		Uniform(1.6Cd)	4.011	-0.654	1.865	0.585
Mooring Top Tension	kN	Exp	3280.0	694.0	1500.0	226.0
		Uniform(1.6Cd)	2987.2	579.5	1492.4	207.2

11. Irregular wave + Dynamic wind condition (Hs=7.1 m, Tp = 12.1 sec, Wind Speed at hub = 11.4 m/sec)

Next, the steady wind of the previous section is replaced by a dynamic wind with smaller mean velocity i.e., 11.4 m/sec rated dynamic wind speed at hub height is added to the same irregular wave condition of 7.1 m significant and 12.1 sec peak period. The rotor thrust forces between physical and numerical models were similarly matched in the range of minimum and maximum wind speeds. For this, the blade pitch angle was fixed to the 11.45 deg. Likewise, blade pitch control was not used in the experiment. The variable speed control mode was turned on in FAST-CHARM3D simulations. Usually, the design of the model rotor part in the Froude-scale-based experiment is very challenging since wind loading is more related to Reynolds number. They typically design the rotor part so that the mean wind thrust is the same as the target value. Fig. 18 and Table 14 show the thrust force between 9.27 m/sec and 13.95m/sec. The thrust value for wind velocity less than 11.23 m/sec in the simulation is slightly smaller than the measurement data. Otherwise, they are almost the same in both simulation and measurement. Table 15 and Figs. 19 and 20 show the surge, heave, pitch, and mooring top tension spectra and

the corresponding statistics. The general trend of the 6DOF motions and the taut-side mooring tension results are similar to those of the previous section. The noticeable change is the increase of low-frequency motions in surge and pitch, which is caused by the low-frequency dynamic wind loading. Again, there is little change in heave mode. Since the mean speed of the dynamic wind is smaller compared to the previous section, the mean surge offset is accordingly reduced. The smaller shift of mooring-line stiffness results in slightly reduced wave-frequency dynamic tension. Such trends are the same between numerical simulation and measured data.
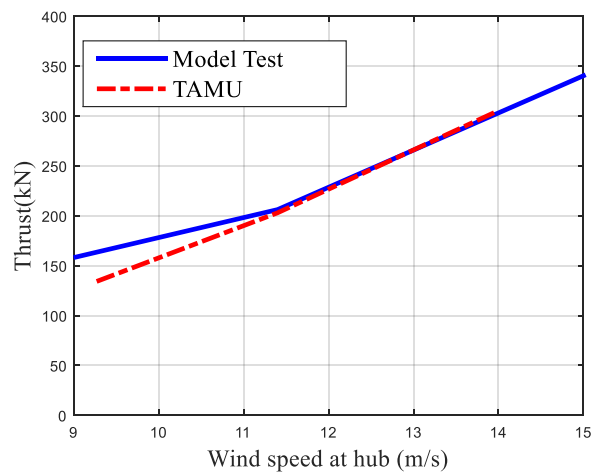

Fig. 18 Thrust force comparison of model test and FAST-CHARM3D simulation between 9.27 m/sec and 13.95 m/sec wind speed at hub height

Table 13 environmental condition in the dynamic wind and the irregular wave case

Title	Unit	Value
Wind Spectrum		NPD
Mean Wind Speed at hub	m/sec	11.4
Maximum/Minimum wind speed at hub	m/sec	13.95 / 9.27
Mean Wind speed at 10m height	m/sec	9.53
Vertical shear exponential		0.0768
Fixed Blade Pitch	deg	11.45

Table 14 Thrust force comparison of model test and FAST-CHARM3D simulation between 9.27 m/sec and 13.95 m/sec wind speed

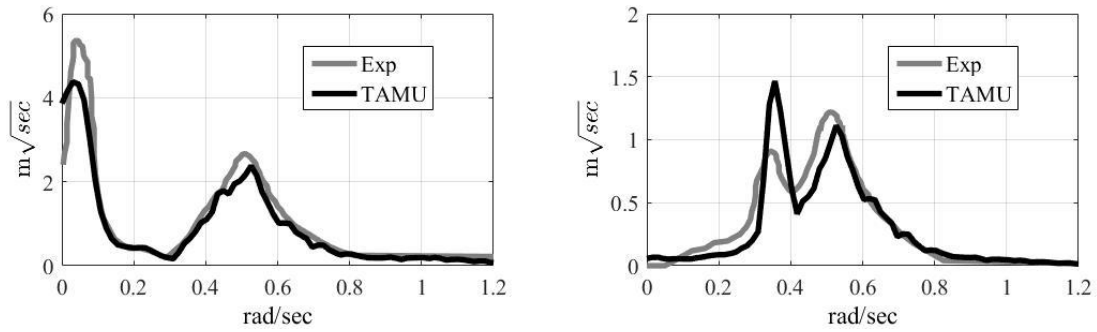| Mean Wind Speed (m/sec)	Thrust in Model Test (kN)	Thrust from FAST (kN)
9.27	163.5	134.2
11.23	202.7	203.0
13.95	302.5	303.4

Fig. 19 Surge SRS (left) and Heave SRS (right) in the irregular wave and dynamic wind condition
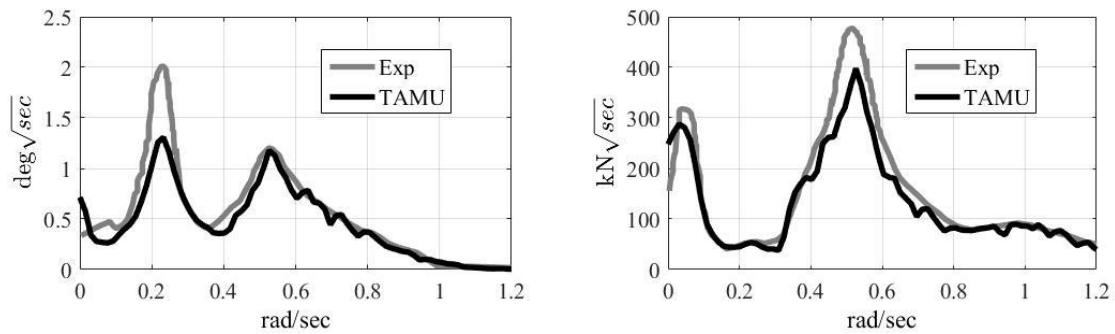

Fig. 20 Pitch SRS (left) and Taut-side mooring top tension SRS (right) in the irregular wave and dynamic wind

Table 15 Surge, heave, and pitch motions and mooring top tension statistics

Title	Unit	Extrapolation	Max	Min	Mean	SD
Surge	m	Exp	12.000	1.300	3.640	1.750
		Uniform(1.6Cd)	10.332	0.018	4.676	1.505
Heave	m	Exp	2.380	-2.110		0.522
		Uniform(1.6Cd)	2.541	-1.718	0.076	0.502
Pitch	deg	Exp	4.710	-2.120	0.814	0.805
		Uniform(1.6Cd)	3.193	-1.746	1.004	0.628
Mooring Top Tension	kN	Exp	3110.0	140.0	1330.0	213.0
		Uniform(1.6Cd)	2701.3	561.8	1356.4	178.2

12. Conclusions

The global performance of the 5MW OC4 semisubmersible floating wind turbine was numerically simulated by using the turbine-floater-mooring fully coupled dynamic analysis program FAST-CHARM3D in time domain. As ocean environments, irregular waves with white-noise and JOSWAP spectrum with and without steady/dynamic winds are considered. The potential-theory-based first- and second-order hydrodynamics results including complete QTFs were calculated through WAMIT in the frequency domain, which were subsequently used in the time-domain simulations. The rotor thrust force generated by the wind in the simulation was matched to that from the model test by adjusting blade pitch angle. The surge, heave, and pitch motions and taut-side mooring top tension results were systematically compared against the corresponding experiment. In the simulation, all the second-order diffraction effects were included.

Additionally, in order to see the effects of wave crest kinematics above MWL, the linear and uniform extrapolation methods were used. They were also compared with no-extrapolation case and the differences among them were discussed. Another sensitivity with column drag coefficient was also tested, which is mostly related to the mean and slowly-varying surge responses. The heave and pitch dynamic motions were little affected by either the wave kinematics extrapolation or column drag coefficient. When steady wind was added to the irregular waves, mean surge and pitch were significantly increased. In particular, large surge offset increased the mooring stiffness so that it could subsequently change motion and mooring dynamics. When dynamic wind was added to the irregular waves, it additionally introduced low-frequency wind loading. The presence of wind also introduced aerodynamic damping. Those numerical-simulation results had good correlation with experimental results for all the cases considered.

References

Bae, Y.H. and Kim, M.H. (2011), "Rotor-floater-mooring coupled dynamic analysis of mono-column-TLP-type FOWT (Floating Offshore Wind Turbine)", *Ocean Syst. Eng.*, **1**(1), 93-109.

Bae, Y.H., Kim, M.H. (2014), "Coupled dynamic analysis of multiple wind turbines on a large single floater", *Ocean Eng.*, **92**, 175-187.

Bae, Y.H. and Kim, M.H. (2014), "Influence of control strategy to FOWT global performance by aero-elastic-control-floater-mooring coupled dynamic analysis", *J. Ocean Wind Energy*, **1**(1), 50-58.

Coulling, A.J., Goupee, A.J., Robertson, A.N., Jonkman, J.M. and Dagher, H.J. (2013), "Validation of a FAST semi-submersible floating wind turbine numerical model with DeepCwind test data", *J. Renew. Sust. Energy*, **5**.

Coulling, A.J., Goupee, A.J., Robertson, A.N. and Jonkman, J.M. (2013), "Importance of second-order difference-frequency wave-diffraction forces in the validation of a fast semi-submersible floating wind turbine model", *Proceedings of the 32th (2013) International Conference on Ocean*, Offshore and Arctic

Engineering Nantes, France.

Coulling A.J., Goupee A.J., Robertson, A.N., Jonkman, J.M., Dagher, H.J. (2013),"Validation of a FAST semisubmersible floating wind turbine model with DeepCwind test data", *J. Renew. Sust. Energ*, in review 2013.

Henderson, A.R., Leutz, R. and Fujii, T. (2002), "Potential for floating offshore wind energy in Japanese waters", *Proceedings of the 12th (2002) International Offshore and Polar Engineering Conference*, Kitakyushu, Japan.

Henderson, A.R., Zaaijer, M., Bulder, B., Pierik, J., Huijsmans, R., Van Hees, M., Snijders, E., Wijnants, G.H. and Wolf, M.J. (2004), "Floating windfarms for shallow offshore sites", *Proceedings of the 14th (2004) International Offshore and Polar Engineering Conference*, Toulon, France.

Jonkman, J.M. and Buhl Jr, M.L. (2004), *FAST user's guide*, National Renewable Energy Laboratory, Rept. NREL/EL-500–29798, Golden, Colorado.

Jonkman, J.M., Butterfield, S., Musial, W. and Scott, G. (2007), *Definition of a 5-MW Reference Wind Turbine for Offshore System Development*, NREL Technical Report No. TP-500-38060.

Kang, H.Y. and Kim, M.H. (2012), "Hydrodynamic interactions and coupled dynamics between a container ship and multiple mobile harbors", *Ocean Syst. Eng.*, **2**(3), 217-228.

Kim, H.C. and Kim, M.H. (2015), "Global performances of a semi-submersible 5MW wind-turbine including second-order wave-diffraction effects", *Ocean Syst. Eng.*, **5**(3), 139-160.

Kim, M.H., Ran, Z. and Zheng, W. (2001), "Hull/mooring coupled dynamic analysis of a truss spar in time domain", *Int. J. Offshore Polar.*, **11**(1), 42-54.

Kim, M.H. and Yue, D.K.P. (1991), "Sum- and difference-frequency wave loads on a body in unidirectional Gaussian seas", *J. Ship Res.*, **35**, 127-140.

Kim, M.H. and Yue, D.K.P. (1989), "The complete second-order diffraction solution for an axisymmetric body. Part 1. Monochromatic incident waves", *J, Fluid Mech.*, **200**, 235-264.

Kim, M.H. and Yue, D.K.P. (1990), "The complete second-order diffraction solution for an axisymmetric body. Part 2. Bichromatic incident waves and body motions", *J. Fluid Mech.*, **211**, 557-593.

Koo, B.J., Goupee, A.J., Kimball, R.W. and Lambrakos, K.F. (2014a), "Model tests for a floating wind turbine on three different floaters", *J. Offshore Mech. Arct..*, **136**(2), 021904.

Koo, B.J., Goupee, A.J., Lambrakos, K. and Lim, H.J. (2014b), "Model test data correlations with fully coupled hull/mooring analysis for a floating wind turbine on a semi-submersible platform", *Proceedings of the 33th (2014) International Conference on Ocean*, Offshore and Arctic Engineering, San Francisco, USA.

Longridge, J. K., Randall, R. E., and Zhang, J. (1996), "Comparison of experimental irregular water wave elevation and kinematic data with new hybrid wave model predictions", *Ocean Eng.*, **23**(4), 277-307.

Masciola, M., Robertson, A.N., Jonkman, J.M., Alexander Coulling, A.J. and Goupee, A.J. (2013), "Assessment of the importance of mooring dynamics on the global response of the deepCwind floating semisubmersible offshore wind turbine", *The International Society of Offshore and Polar Engineers.*

Musial, W.D., Butterfield, S. and Boone, A. (2004), *Feasibility of floating platform systems for wind turbines*, Paper presented at the 4second AIAA Aerospace Sciences Meeting and Exhibit, Reno, NV.

Robertson, A., Jonkman, J., Vorpahl, F., Popko,W., Qvist, J., Frøyd, L., Chen, X., Azcona, J., Uzunoglu, E., Guedes Soares, C., Luan, C., Yutong, H., Pengcheng, F., Yde, A., Larsen, T., Nichols, J., Buils, R., Lei, L., Anders Nygard, T., Manolas, D., Heege, A., Ringdalen Vatne, S., Ormberg, H., Duarte, T., Godreau, C., Fabricius Hansen, H., Wedel Nielsen, A., Riber, H., Le Cunff, C., Abele, R., Beyer, F., Yamaguchi, A., Jin Jung, K., Shin, H., Shi, W., Park, H., Alves, M. and Guérinel, M. (2014), "Offshore code comparison collaboration continuation within IEA wind task 30: phase II results regarding a floating semisubmersible wind system", *Proceedings of the 33th (2014) International Conference on Ocean*, Offshore and Arctic Engineering, San Francisco, USA.

Roddier D., Cermelli C., Aubault, A. and Weinstein A. (2010), "WindFloat: A floating foundation for offshore wind turbines", *J. Renew. Sust. Energy*, **2**.

Tahar, A. and Kim, M.H. (2003), "Hull/mooring/riser coupled dynamic analysis and sensitivity study of a tanker-based FPSO", *J. Appl. Ocean Res.*, **25**(6), 367-382.

Tong, K.C. (1998), "Technical and economic aspects of a floating offshore wind farm", *J. Wind Eng. Ind. Aerod.*, **74-76**, 399-410.

Wayman, E.N., Sclavounos, P.D., Butterfield, S., Jonkman, J. and Musial, W. (2006), "Coupled dynamic modeling of floating wind turbine systems", *Proceedings of the Offshore Technology Conference*, Houston, TX.

Yang, C.K. and Kim, M.H. (2010), "Transient effects of tendon disconnection of a TLP by hull-tendon-riser coupled dynamic analysis", *Ocean Eng.*, **37**(8-9), 667-677.

Zhao, W. and Wan, D. (2015), "Numerical study of interactions between phase ii of oc4 wind turbine and its semi-submersible floating support system", *J. Ocean Wind Energy*, **2**(1), 45-53.